The Effects of Soil Representation in WRF–CLM on the Atmospheric Moisture Budget

ELI J. DENNIS[a] AND E. HUGO BERBERY[a]

[a] CISESS, Earth System Science Interdisciplinary Center, University of Maryland, College Park, College Park, Maryland

ABSTRACT: Soil hydrophysical properties are necessary components in weather and climate simulation, yet the parameter inaccuracies may introduce considerable uncertainty in the representation of surface water and energy fluxes. This study uses seasonal coupled simulations to examine the uncertainties in the North American atmospheric water cycle that result from the use of different soil datasets. Two soil datasets are considered: the State Soil Geographic dataset (STATSGO) from the U.S. Department of Agriculture and the Global Soil Dataset for Earth System Modeling (GSDE) from Beijing Normal University. Two simulations are conducted from 1 June to 31 August 2016–18 using the Weather Research and Forecasting (WRF) Model coupled with the Community Land Model (CLM) version 4 and applying each soil dataset. It is found that changes in soil texture lead to statistically significant differences in daily mean surface water and energy fluxes. The boundary layer thermodynamic structure responds to these changes in surface fluxes resulting in differences in mean CAPE and CIN, leading to conditions that are less conducive for precipitation. The soil-texture-related surface fluxes instigate dynamic responses as well. Low-level wind fields are altered, resulting in differences in the associated vertically integrated moisture fluxes and in vertically integrated moisture flux convergence in the same regions. Through land–atmosphere interactions, it is shown that soil parameters can affect each component of the atmospheric water budget.

KEYWORDS: Soil moisture; Water budget/balance; Land surface model

1. Introduction

Soil science plays an increasingly prominent role in hydrology and Earth system science, partially motivating the creation of the International Soil Modeling Consortium (Vereecken et al. 2016), which, among other activities, promotes the study of soil processes within Earth system modeling frameworks. However, many challenges still exist: the implementation of soil processes in land surface models (LSMs) has been shown to introduce further GCM dependence on resolution (Bosilovich and Sun 1998), while high variability is shown between the use of different combinations of soil textures, soil parameters, and hydraulic parameterizations (Verhoef and Egea 2014). Other results suggest that soil hydrophysical properties (Kishné et al. 2017) are regionally specific. The solutions to these challenges necessitate simultaneous observations of soil moisture, surface fluxes, and multiple horizons of soil properties (Mu et al. 2021)—an observational dataset that is likely difficult to achieve on a global scale.

Despite these obstacles, the evolving soil sciences community has made remarkable strides in developing high-resolution global soil datasets (Hengl et al. 2017; Lannoy et al. 2014; Shangguan et al. 2014). Estimates of soil hydrophysical properties have been compiled from novel regional measurement techniques (Lu et al. 2020), physics-based relationships (Lehmann et al. 2018; Or and Lehmann 2019; Zhang et al. 2018), and statistical mechanisms such as random forests (Szabó et al. 2019) and other pedotransfer functions (PTFs; van Looy et al. 2017). These are used to derive high-resolution soil hydrophysical property maps (Dai et al. 2019a; Chaney et al. 2019), which can be used to enhance coupled and uncoupled land surface model (LSM) simulations. See Dai et al. (2019b) for a review of global soil datasets used in Earth system models.

Despite the availability of global high-resolution soil hydrophysical property datasets, many LSMs remain dependent on look-up tables to associate soil textural categories with empirically derived hydrophysical properties. Look-up tables, while computationally efficient, require soil hydrophysical properties to remain discrete and linked to broad estimates of soil texture rather than continuous evolving quantities. Furthermore, the usage of a lookup table assumes (i) that soil properties are globally transferable, which often is not the case, and (ii) that it is dependent on soil texture maps. Thus, at typical coupled modeling resolutions, the prescriptive soil texture categories can vary significantly between prominent datasets.

Furthermore, in the context of coupled modeling, soil hydrophysical properties and the choice of PTFs have been shown to impact soil moisture that in turn affects surface water and energy fluxes (Ek and Cuenca 1994; Weihermüller et al. 2021), surface heat fluxes (Peters-Lidard et al. 1998), and PBL evolution (Breuer et al. 2012; Dennis and Berbery 2021, hereafter DB21; Kim and Entekhabi 1998; Pan and Mahrt 1987; Ek and Cuenca 1994). Further, land–atmosphere interactions (Seneviratne et al. 2010; Koster et al. 2004; Dirmeyer 2011; Santanello et al. 2018) are dependent on surface water and energy fluxes; therefore, if soil hydrophysical properties influence surface fluxes, they can also influence land–atmosphere interactions. The so-called "terrestrial leg" of land–atmosphere coupling links soil moisture via surface

---

processes (Dirmeyer 2011) to surface latent and sensible heat fluxes, while the atmospheric leg expands that relationship to describe the effect of surface fluxes on PBL evolution, clouds, and precipitation (Dirmeyer et al. 2014). The specific role of surface properties in land–atmosphere coupling (including the role of soil texture and soil hydrophysical properties) has received less attention than, for instance, the relationship between soil moisture and precipitation (Hohenegger et al. 2009; Findell and Eltahir 1997; Eltahir 1998).

At and beneath the surface, soil hydrophysical properties play a vital role in the terrestrial water budget, affecting evapotranspiration, groundwater recharge, and runoff. Clayey soils require more time to percolate water to lower levels, which can lead to increases in runoff, pooling, and evapotranspiration of standing water (Duffkova 2013). Sandy soils, on the other hand, quickly absorb and transmit moisture after rainfall (Duffkova 2013). Subsurface runoff generally increases for nonvegetated surfaces versus vegetated surfaces (Liao et al. 2016), and for compacted soil surfaces versus aerated and natural surfaces (Prats et al. 2021). Groundwater recharge (GR) is also dependent on soil texture, with GR in finer soils being more sensitive to climatic conditions than GR in coarse soils (Wang et al. 2015). These mechanisms work to distribute soil moisture, which is critical to linking the land surface with the atmosphere.

After soil moisture is distributed, land–atmosphere interactions have been shown to create environments more (or less) conducive for convection to occur. Soil moisture conditions have been shown to affect thermodynamic instability (Holt et al. 2006; Yin et al. 2015) and develop cross-boundary mesoscale circulations providing vertical motion and preferred initiation locations (Avissar and Liu 1996; Zheng et al. 2021; Lee et al. 2019). Similarly, the land properties can enhance or diminish the horizontal transport of moisture (Lee and Berbery 2012a; Lee et al. 2013; Yang and Dominguez 2019), affecting vertically integrated moisture flux convergence— a critical component in the atmospheric water budget (Rasmusson 1968; Roads et al. 1994; Trenberth et al. 2007). While these impacts have been studied from a general land surface perspective, the specific role of soil texture in these relationships has not been examined as much.

This study aims to connect the atmospheric portion of land–atmosphere coupling to the impact of soil texture-modulated surface fluxes. It is hypothesized that the soil's hydrophysical properties, via their influence on surface fluxes, will affect the thermodynamic instability [i.e., convective available potential energy (CAPE) or convective inhibition (CIN)], as well as moisture transports (i.e., atmospheric circulation), ultimately influencing the atmospheric water budget. This study represents a follow-on to an earlier study: DB21. DB21 examined the soil properties' role in determining surface water and energy fluxes and near-surface states. This study advances their analysis to focus on the PBL evolution, thermodynamic environments for precipitation (i.e., atmospheric stability), dynamic precursors to precipitation (i.e., moisture transports), and the atmospheric water budget. To this end, we compare the two sets of summer WRF simulations described in DB21 using different soil texture datasets: one using the State Soil

Geographic Dataset (STATSGO; NRCS 2012) soil texture dataset and the other using the Global Soil Dataset for Earth System Modeling (GSDE; Shangguan et al. 2014). The experimental design is outlined in section 2, followed by descriptions of the soil texture datasets. Section 3 will validate the model simulations using in situ measurements and reanalysis and discuss the model internal variability. Section 4 will highlight the soil-parameter-induced differences in the thermodynamic and dynamic environment and relate those differences to the atmospheric water cycle. Finally, section 5 provides our concluding remarks.

2. Experimental setup

a. Model design

The model configuration and simulations are the same ones used by DB21. We used WRF's Advanced Research version (WRF-ARW v3.9; Skamarock et al. 2008) to carry out simulations over three summers (JJA 2016–18) to examine near-surface processes related to soil physics. In this study, we investigate how atmospheric processes can be related to soil physics. The model domain covers the continental United States (CONUS), Mexico, northern Central America, and southern Canada (see Fig. 1) at a 15-km horizontal resolution. There are 51 vertical layers, with 13 in the lowest 1 km to improve boundary layer representation. The model parameterizations include a single-moment microphysics scheme (Thompson et al. 2008), the Rapid Radiation Transfer Model (Iacono et al. 2008), and the Betts–Miller–Janjić convective parameterization scheme (Janjić et al. 2001). The PBL is represented using Mellor–Yamada–Nakanishi–Niino (MYNN) 2, a second-order closure, a local PBL scheme (Nakanishi and Niino 2006), and the compatible MYNN surface layer scheme to account for the interface between the land surface and the PBL. The combination of parameterizations was chosen based on previous literature (e.g., Lee and Berbery 2012b; Lee et al. 2013; Müller et al. 2014) combined with the authors' previous experiences.

As discussed in DB21, WRF is coupled with the land surface model, Community Land Model version 4 (CLMv4, hereafter CLM). CLM interacts with the atmospheric model to establish the lower boundary conditions related to the surface water and energy budgets. It represents the soil–atmosphere–vegetation nexus using a resistance formulation and accounts for soil hydraulics using a classical understanding of fluid movement within porous media (e.g., Richards 1931). CLM has 10 vertical soil layers increasing in thickness with depth and extending down to 3.42 m. A full technical description of CLM can be found in Oleson et al. (2010). CLM's positive performance has been reported thoroughly in the literature, for example, against the NLDAS testbed experiments (e.g., Xia et al. 2012; Cai et al. 2014; Xia et al. 2017, etc.) and in both offline and coupled mode (to CAM3.0) for climate-scale processes (e.g., Lawrence et al. 2007, 2011).

Representing soil physics requires knowing their hydraulic— or hydrophysical—properties. In models, they are usually derived as parameters specific to a soil texture classification.
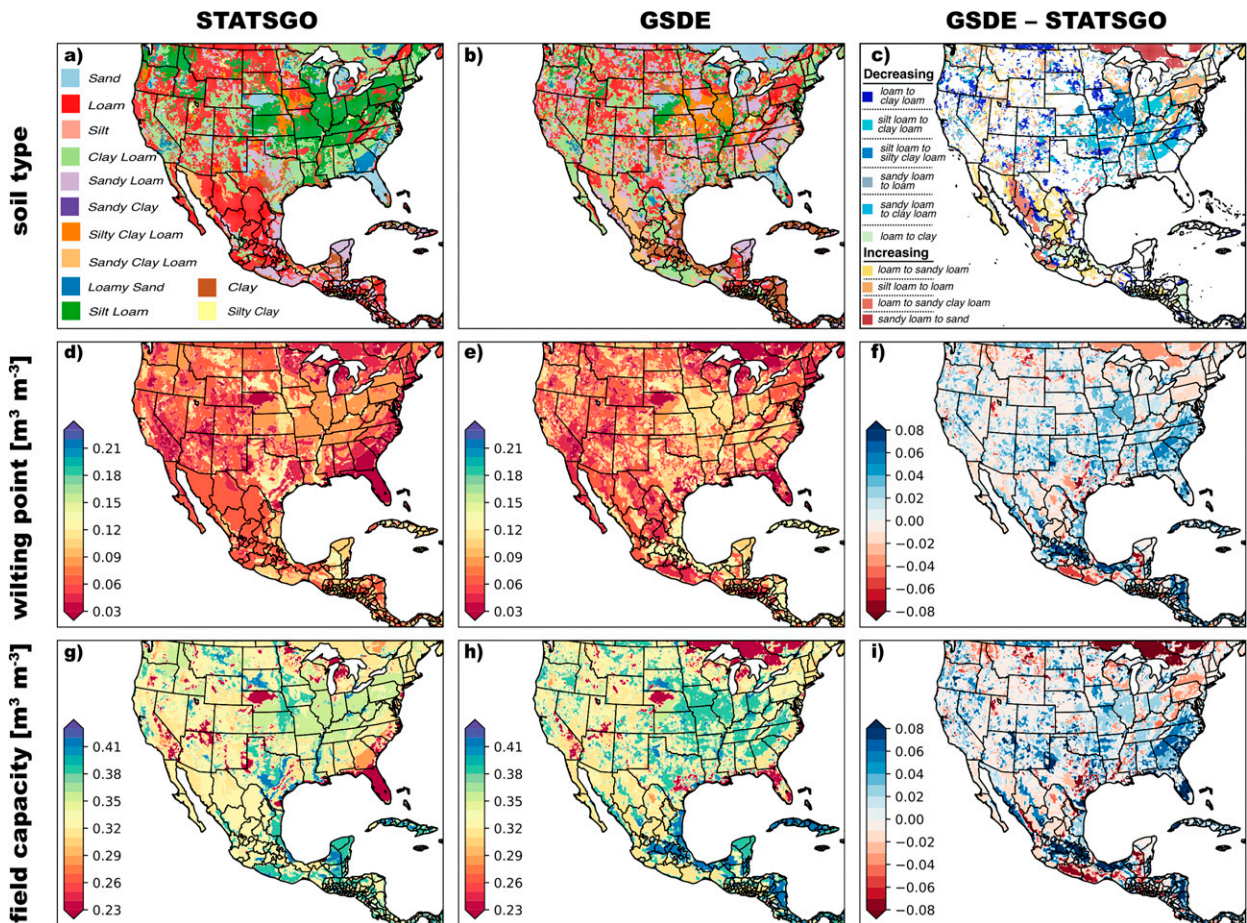
FIG. 1. Soil category assignments are shown for (a) STATSGO, (b) GSDE, and (c) for the 10 most common soil category transitions. The soil categories [(a) and (b); adapted from DB21, their Figs. 1a and 1b, respectively] are defined by the key in (a). The transitions in (c) are organized by change in grain size with larger-to-smaller (i.e., decreasing grain size) transitions in cool colors, and smaller-to-larger transitions (i.e., increasing grain size) in warm colors. The assigned wilting point is shown for (d) STATSGO and (e) GSDE, as well as (f) the differences (GSDE − STATSGO). The field capacity for (g) STATSGO and (h) GSDE is shown, as well as (i) the differences [GSDE − STATSGO) in field capacity.

Then, a lookup table with parameters that correspond to each soil texture category is used. The lookup table parameters are based on empirical relationships obtained in laboratory experiments (e.g., Cosby et al. 1984). This method assumes that categories are universal (i.e., sand in one area is the same as sand everywhere) and that they can be transferrable to the real world—a topic that is important for soil science research. The lookup table approach has the advantage that only the soil texture maps and the lookup table are needed to define all the soil's hydrophysical properties; therefore, it is computationally inexpensive. However, the soil system and the land–atmosphere coupling do become dependent on the external soil texture databases.

Our goal is to determine the impact of these soil databases via their soil hydrophysical properties on land–atmosphere interactions and the atmospheric water budget. It is well understood that vegetation has a significant effect on surface fluxes, as well. Therefore, the simulations have been given the same vegetation assignments to avoid vegetation dependencies

when assessing the impact of soil hydrophysical properties. This approach allows us to isolate the effect of the soils more easily despite the presence and role of vegetation.

b. Soil databases

During the preprocessing stage for WRF the model's grid is defined. Its static fields are assigned to each grid space (i.e., soil type, vegetation type, topographical features) based on the provided databases. For a complete description of this process, please refer to DB21 and the supporting literature. The default soil texture classifications in WRF are provided using the USDA STATSGO soil dataset (NRCS 2012). For regions outside of the United States, the Food and Agriculture Organization (FAO) Soil Map of the World (FAO/UNSECO 1971), which is about 5-km grid spacing, is employed. Within the United States, STATSGO is used. STATSGO was based initially on the FAO Soil Map of the World. Since then, it has expanded to include multiple additional high-resolution surveying campaigns supplemented

with Landsat data over CONUS and U.S. territories, where its current resolution is about 1 km.

As in DB21, the second soil texture database in this study, GSDE, was also based initially on the FAO Soil Map of the World. GSDE represents a modern alternative to STATSGO for simulation studies inside the United States, as each represent plausible estimations of soil properties and soil texture in this region. It uses numerous global surveying campaigns complemented with advanced statistical regridding procedures and machine learning to infer the soil parameters in undersurveyed regions (Shangguan et al. 2014; Dai et al. 2019a). It is provided at 1 km globally and offers eight vertical levels of soil characteristics. GSDE provides 1-km resolution globally as opposed to STATSGO's 1-km resolution only over CONUS and U.S. territories. DB21 showed that the differences in soil classification between these two datasets are not randomly distributed, but, instead, they exist in coherent areas of reduced/increased soil grain size, which allows their impacts to be projected onto regional scales (see Fig. 1c).

Figures 1a and 1b present the model soil classifications as portrayed by the STATSGO database and the GSDE database. As shown in DB21, the primary soil classification in the midwestern United States (Midwest) is silt loam (green) in the STATSGO map. In contrast, in the GSDE map, many categories can be identified: silty clay loam (orange), sandy loam (light purple), and loam (red). Each of these differences, or "transitions," represents a change in soil hydrophysical properties (i.e., a difference in how the soil interacts with water). Many differences can be identified between Figs. 1a and 1b, but the 10 most common transitions are highlighted in Fig. 1c. Notice a continuous area of transitions in Fig. 1c that extends from the Texas–Arkansas border northeastward into Pennsylvania, the area here referred to as the Midwest. Most of these transitions represent a decrease in average soil grain size.

Figure 1 also shows the distribution of selected soil hydrophysical parameters as they have been assigned from the lookup table. Figures 1d and 1e show the wilting point (i.e., the lower limit for soil water storage under normal conditions). GSDE has the higher wilting point values (Fig. 1e, lighter yellow colors) throughout Missouri, Illinois, Indiana, Kentucky, and Ohio, as compared to the lower values in the same area in the STATSGO dataset (Fig. 1d, mostly orange colors). Similarly, the third row in the figure shows the field capacity (i.e., the maximum amount of moisture a soil can hold after free drainage occurs). Notice the higher field capacity values in GSDE (Fig. 1h, mostly blue colors) throughout the same region as the wilting point example compared to the lower values in the STATSGO dataset (Fig. 1g, light green colors).

The smaller size grains in GSDE imply that both field capacity and wilting point increase. Therefore, most of the map (Figs. 1f,i) shows that the differences in GSDE minus STATSGO hydrophysical properties have positive differences. As with wilting point and field capacity, other hydrophysical properties are connected to each soil textural classification. Thus, when one changes the locations of the soil texture categories one is changing the spatial distribution of soil hydrophysical properties, which affects the way the soil

interacts with the surface and subsurface moisture. In the next section, we assess the impact of using these two soil datasets in separate regional climate simulations to support this assertion.

3. Model performance

Performance of the model is examined at two-time scales: the diurnal cycle and the seasonal means. The first step is to contrast the diurnal cycle of the model's surface fluxes against selected AmeriFlux flux towers. Then, the evaluation of the mean fields is done by contrasting mean fields with observationally based forcings employed in land data assimilation systems. In our study, the substance lies in the differences produced by changes in soil categories between the models themselves. Thus, it is not an attempt to determine which model configuration performs better. Instead, comparing point measurements to model simulations is helpful to assess if the model simulations are sufficiently realistic.

a. AmeriFlux towers

To confirm that the model physics can reproduce plausible physical patterns, we compare the regional climate model simulations against observations. To this end, the diurnal cycle of surface latent and sensible heat fluxes in the WRF experiments are contrasted against data from three AmeriFlux towers (Fig. 2). An inverse distance-weighted average was used to interpolate the model data to each flux tower's location. The sites were chosen based on availability and continuity of data. They are the U.S.-ARM Central Facility in Oklahoma (Biraud et al. 2020), the U.S.-MMS in central Indiana (Novick and Phillips 2020), and the U.S.-IB1 in the rural suburbs of Chicago, Illinois (Matamala 2019). Table 1 presents the characteristics of each tower location. This comparison illustrates the model's ability to reproduce the diurnal cycle of surface fluxes without declaring which configuration is superior. Instead, it is meant to illustrate that the model is of sufficient quality to address the role of soil texture assignment in altering the surface fluxes. The role of other surface energy balance terms was also considered, but the components of radiation showed only small differences in the mean diurnal cycle (not shown) leading to a balance primarily between latent and sensible heat fluxes.

The U.S.-ARM site has a soil texture identified as silt loam, with a land cover of cropland that cycles between winter wheat, alfalfa, and soybeans (see Table 1). The model's land use assignment for all experiments identifies the site as grassland. The WRF-STATSGO simulation, hereafter WRF$_S$, has the appropriate soil texture for that location (silt loam). In contrast, the WRF-GSDE simulation, hereafter WRF$_G$, specifies clay loam—a relative reduction in soil grain size. According to DB21, smaller soil grains can reduce latent heat flux and increase sensible heat flux relative to the simulation employing STATSGO. Figure 2a shows the U.S.-ARM flux tower's JJA 2016–18 mean diurnal cycle of latent and sensible heat fluxes and compares them to WRF$_S$ and WRF$_G$ simulations. In terms of latent heat flux (solid lines), both model and observed diurnal cycles experience consistent timing in the maximum and minimum values, with latent heat flux
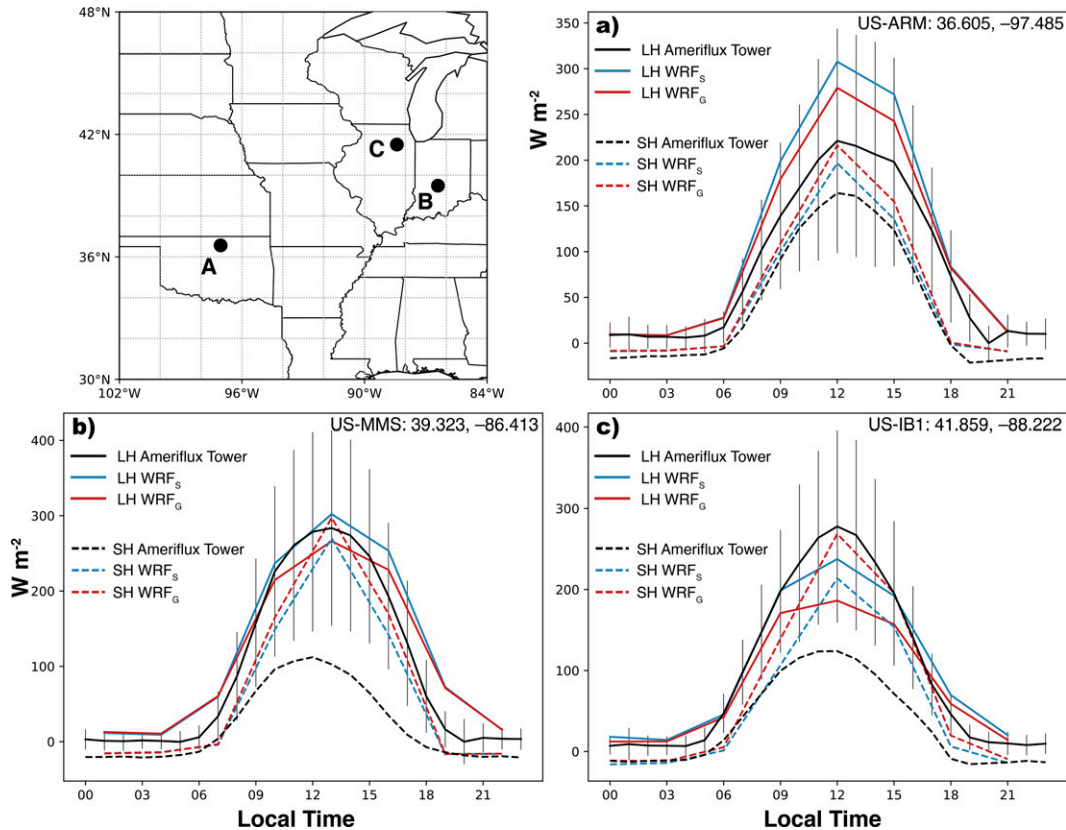
FIG. 2. The diurnal cycle of latent (W m^{-2}) and sensible heat flux (W m^{-2}) the model simulations are compared to AmeriFlux tower in situ flux measurements. The location of each tower is given as lat/lon coordinates, and it is shown in the inset map. Solid lines represent latent heat flux, while dotted lines show sensible heat flux. The AmeriFlux towers (black) are compared to WRF$_S$ (blue) and WRF$_G$ (red) at each flux tower location. Vertical black lines represent one standard deviation from the observed latent heat flux curve.

increasing throughout the morning hours from about 0700 local time (LT) until about 1200 LT and decreasing as the sun sets around 1800 LT. The WRF$_S$ simulation with silt loam soil type experiences the greatest average latent heat flux at the diurnal maximum (about +300 W m^{-2} at 1200 LT). In this location, the WRF$_G$ simulation has a smaller soil grain assignment, and it shows reduced average latent heat flux throughout the diurnal cycle compared to WRF$_S$. In terms of sensible heat flux, the WRF$_G$ simulation has an increased diurnal

maximum compared to the WRF$_S$ (+15 W m^{-2}) and the in situ measurements (+50 W m^{-2}). While differences are apparent between the model simulations and the observed diurnal fluxes, the model simulations fall within ±1 standard deviation of the observed mean (vertical lines in Figs. 2a–c) indicating a similar behavior between the simulations and observations.

Figure 2b presents the U.S.-MMS AmeriFlux site (39.323°N, 86.413°W). This site's information does not include soil type, but it is in a deciduous broadleaf forest, (see Table 1). The

TABLE 1. Describes the characteristics of each AmeriFlux tower site according to the site metadata compared to the characteristics of the associated grid spaces in both model environments.

Location (lat, lon)	Source	Soil type	Vegetation type
U.S.-ARM (36.605°N, 97.485°W)	Flux tower	Silt loam (nearby)	CROP; winter wheat, soy, alfalfa
	STATSGO	Silt loam	Grasslands
	GSDE	Clay loam	Grasslands
U.S.-MMS (39.323°N, 86.413°W)	Flux tower	Unspecified	Deciduous broadleaf forest; >60% coverage
	STATSGO	Silt loam	Deciduous broadleaf forest
	GSDE	Loam	Deciduous broadleaf forest
U.S.-IB1 (41.859°N, 88.222°W)	Flux tower	Silty clay loam	CROP; corn, soybean
	STATSGO	Silt loam	Urban, cropland
	GSDE	Silty clay loam	Urban, cropland

diurnal cycles of latent heat flux in both model simulations are very similar to the observations at this site, rising to about 275 W m^{-2} at the peak and falling off to near 0 W m^{-2} during the nighttime hours, and during that time fall within one standard deviation of the observed mean. Sensible heat flux, however, shows more of a difference between the two model simulations and the in situ measurements. The nonlinear characteristics of canopy shading and subcanopy turbulence are difficult to account for in models (Fisher and Koven 2020; Bonan et al. 2018). Forest dynamics could then contribute to the differences in sensible heat flux between the simulations and in situ measurements.

The third site, U.S.-IB1 (Fig. 2c), has silty clay loam as the observed soil type and cropland as the observed vegetation coverage (corn and wheat; see Table 1). In this instance, GSDE has the appropriate soil type assignment (silty clay loam), while STATSGO's is somewhat different (silt loam). Curiously, WRF$_G$ has a lower performance than WRF$_S$ in terms of latent and sensible heat flux biases. Both simulations have similar timing of the diurnal cycle, but both overestimate the magnitude of sensible heat flux and underestimate the magnitude of latent heat flux at the diurnal peak. Despite underestimating the latent heat flux, the simulated diurnal cycles fall within one standard deviation of the mean. Figure 2c shows that with finer soil grains in GSDE compared to STATSGO, the WRF$_G$ simulation yields reduced latent heat flux values and increased sensible heat flux following the surface energy balance.

b. NLDAS2 forcing

It is also relevant to examine the spatial structure of the surface variables in the model simulations. To this end, we employ the North American Land Data Assimilation System version 2 (NLDAS2) forcing (Cosgrove et al. 2003) as a proxy for observations. We selected 2-m temperature, 2-m specific humidity, and precipitation to compare against the WRF Model products from this dataset. Due to differences in grid spacing, the WRF Model data were bilinearly interpolated to the NLDAS2 grid (~12-km grid spacing).

The NLDAS2 nonprecipitation forcing data are derived from the North American Regional Reanalysis (NARR; Mesinger et al. 2006) analysis fields but are spatially interpolated to the finer 1/8° NLDAS2 grid. Additionally, the forcing data are temporally disaggregated from the 3-hourly NARR data to the NLDAS hourly time step. The NLDAS precipitation data are a temporal disaggregation of a CPC gauge-based daily precipitation (Xie et al. 2007), combined with Doppler radar data, CMORPH data, and 3-hourly NARR data in a way that reflects the strengths of each dataset on the NLDAS grid (Cosgrove et al. 2003).

Figure 3a presents mean (JJA 2016–18) precipitation from the NLDAS forcing dataset. The western United States is mostly dry during this period, with most areas experiencing 1 mm day^{-1} or less. While the monsoon precipitation in northwestern Mexico is strongest in JAS, its signal is already detected in JJA. In the central United States, the characteristic gradient of increasing precipitation from the front range of

Colorado eastward into the Midwest is present, along with slightly elevated precipitation values along the eastern and southern U.S. coastal regions.

Most models tend to have more difficulties in reproducing summer precipitation due to their dependence on imperfect parameterizations. Models often overproduce precipitation in regions near topography. In addition, the propagation speed of convective systems is reduced, resulting in increased daily precipitation values, especially in mountainous regions (Tripathi and Dominguez 2013; Yun et al. 2020; Navale et al. 2020). This is also the case of the WRF Model. The differences (WRF$_S$ − NLDAS) in mean (JJA 2016–18) precipitation are shown in Fig. 3b. The overall model precipitation pattern is like that in observations (not shown), but regional biases are noticed. The western mountain region exhibits positive precipitation anomalies, while the opposite is true in most of the United States east of the Continental Divide. Negative biases are also observed along the eastern and southern U.S. coasts, reaching precipitation of about −2 mm day^{-1}.

Figure 3c depicts the (JJA 2016–18) mean 2-m temperature from the NLDAS2 forcing dataset. The climatological features show high temperatures in the south-central United States and in the southwestern U.S. desert regions, with cooler values in the Rocky Mountains and the Pacific Northwest. Comparing WRF$_S$ to NLDAS2 forcing (Fig. 3d), the WRF$_S$ simulation has a warm bias (from +1 to +2 K) in the eastern and central United States and a cool bias (from −2 to −3 K) in the Rocky Mountains. Because the resolutions of NLDAS2 and the WRF simulations are similar, we expect differences due to grid interpolation to be negligible in extreme topography areas (i.e., the Rocky Mountains), yet some differences may arise.

In Fig. 3e, the mean 2-m specific humidity is shown from the NLDAS2 forcing. The climatology shows a northwest-to-southeast gradient of increasing specific humidity across the CONUS region, with maximum values along the Gulf Coast and southern Atlantic Coast states. Compared to the NLDAS2 forcing, the WRF$_S$ simulation reveals a widespread dry bias (from −1 to −2 g kg^{-1}) that occupies most of the eastern part of the United States, with smaller positive biases (from 0 to +1 g kg^{-1}) existing in the western states.

The midwestern U.S. environment in the WRF$_S$ simulation is both slightly warmer and slightly drier than the NLDAS2 forcing data. Still, compared to other model simulations, it is within a reasonable range. The WRF$_G$ simulation displays an environment more like WRF$_S$ than it is to NLDAS, but with even warmer and drier conditions in the Midwest. These variables are compared between simulations in DB21 (see their Fig. 8). This study aims not to rank the simulations in terms of accuracy but instead to investigate the implications of their soil-induced differences.

c. Model variability

In an ensemble strategy, multiple instances of similar physical responses given different initial conditions are more robust than single simulations, increasing the likelihood that the system's responses are due to imposed conditions rather
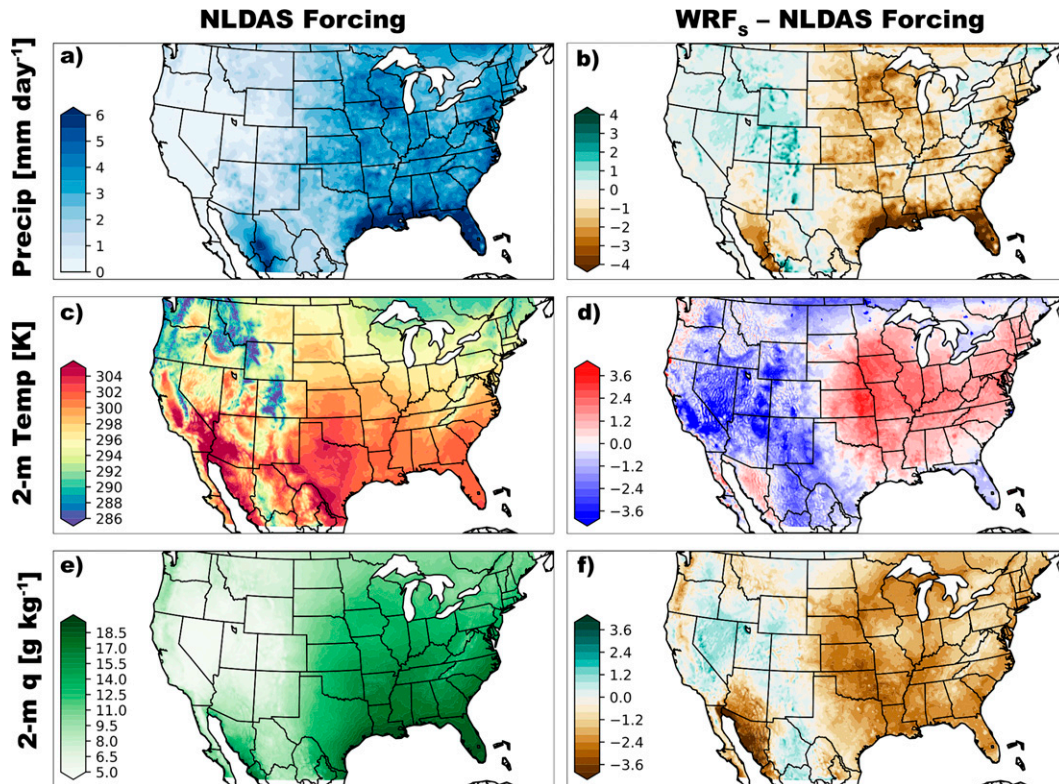
NLDAS Forcing **WRF$_S$ − NLDAS Forcing**

FIG. 3. Meteorological fields from the NLDAS Forcing (a) precipitation (mm day^{-1}), (c) 2-m temperature (K), and (e) 2-m specific humidity (g kg^{-1}). Differences (WRF$_S$ − NLDAS forcing) bilinearly interpolated to the NLDAS grid: (b) precipitation (mm day^{-1}), (d) 2-m temperature (K), and (f) 2-m specific humidity (g kg^{-1}).

than an unknown factor. Even though our set of simulations is small, there are no prominent outlying ensemble members lending confidence that the systems are responding similarly to the imposed conditions despite different initial conditions. Given the dependence of ensemble-mean values on the individual members and to ensure that collectively they represent an adequate ensemble distribution, we evaluate the simulations for key variables at intraseasonal and interannual scales.

Considering the intraseasonal variability, Fig. 4 shows estimated probability distribution functions of daily mean values for both domain-averaged precipitation and domain-averaged latent heat flux. Concerning precipitation, each month reports similar distributions of daily values. July has the narrowest distribution (Fig. 4a), indicating the most similarity day to day, with mean values near 3 mm day^{-1}. June experiences the widest distribution with daily values approaching 6 mm day^{-1} on the upper tail of the distribution and a cluster of nonprecipitating days. While the daily mean values in August are most like the entire simulation mean distribution (black line).

The daily latent heat flux (Fig. 4b) displays a different intraseasonal behavior compared to the corresponding for daily precipitation. Domain-averaged daily latent heat values decrease as the season progresses: the highest likelihood of high values is found in June, midrange values in July, and the likelihood of lower latent heat flux values is found in August. The complete simulation-average daily values (black line)

have a reduced peak but are much broader to encompass the month-to-month variability.

Contrasting interannual variability instead (Figs. 4c,d), precipitation and latent heat flux show similar and related patterns. First, for precipitation, Fig. 4c shows that 2017 is skewed toward the lower end of daily mean precipitation values, while 2018 is skewed slightly toward the upper end of the distribution. The daily values or precipitation from 2016 represent the best estimate of the ensemble mean. The distribution of interannual daily latent heat flux (Fig. 4d) echoes the same pattern as the distribution of interannual daily precipitation with less latent heat flux occurring each day in 2017, while 2018 experiences slightly higher than normal latent heat flux each day. The distributions of daily mean precipitation and latent heat flux can be interpreted in two ways: 1) if more precipitation occurs, there could be more moisture available to transmit from the land surface to the atmosphere, increasing latent heat flux, or 2) if more latent heat flux occurs, there could be more conducive conditions for precipitation to occur leading to increased precipitation.

4. Changes in the environment

a. Thermodynamic drivers

Atmospheric instability is the primary thermodynamic forcing of summer precipitation. Areas with more CAPE and
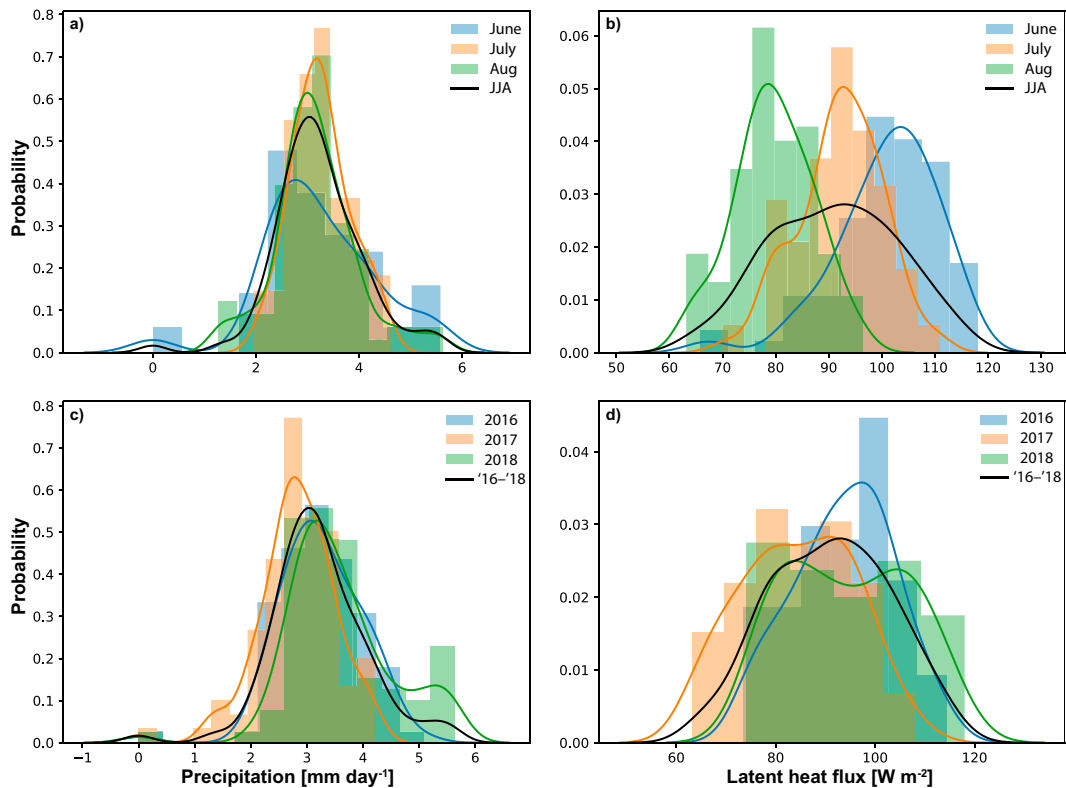
FIG. 4. The interannual and intraseasonal variability is displayed in terms of the distributed probability of occurrence of domain-averaged daily (a),(c) precipitation and (b),(d) latent heat flux. Intraseasonal variability is shown as histograms and approximated distributions of daily mean values in June (blue), July (orange), and August (green), with the black line representing the full simulation mean. Interannual variability is shown as distribution of the probability of daily mean values in 2016 (blue), 2017 (orange), and 2018 (green), again with the black lines representing the full simulation mean.

smaller CIN are more conducive environments for initiating and sustaining precipitating systems. CAPE and CIN are highly dependent on low-level temperature and moisture and on the evolution of the PBL; therefore, because soil properties affect the surface water and energy fluxes, they influence atmospheric stability also.

The spatial patterns of latent and sensible heat fluxes are shown in Fig. 5. The WRF$_S$ simulation mean latent heat flux (Fig. 5a) exhibits lower western United States values, with higher values in the eastern United States. In the Midwest, values approach 150 W m^{-2} (Fig. 5a). The differences between the two simulations (WRF$_G$ − WRF$_S$; Fig. 5b) are consistent with the reduction in soil grain size—smaller grains in GSDE lead to reduced latent heat flux, as illustrated in the Midwest by the negative differences of about −15 W m^{-2}, or about 10% of the climatological value. This is like what is shown in DB21 (see their Figs. 8a,b). The differences across much of the domain are significant at the 95% confidence interval ($p = 0.05$) denoted by the stippled area in Figs. 5b and 5d. Note that these differences in surface fluxes represent full period mean values, including nighttime values suggesting that for a daytime-only calculation the differences are probably much larger (perhaps even 2 times). These differences

in surface fluxes lead to differences in 2-m specific humidity of about −2 g kg^{-1} in the same region (DB21, see their Fig. 8c).

When incoming energy can no longer remove moisture from the soil, it is partitioned between sensible heat flux, outgoing longwave radiation, and ground heat flux. Therefore, mean sensible heat flux displays a similar (but opposite) pattern in the WRF$_S$ simulation (Fig. 5c): larger values in the western United States and lower values in the eastern United States. Differences between the two simulations (Fig. 5d) reveal an increase in sensible heat flux collocated with the soil-texture-related negative differences in latent heat flux in the Midwest region, approaching about 15 W m^{-2} or about 15%–20% of the climatological value in that region. These differences in sensible heat flux are collocated with positive differences in 2-m temperature of about +2 K (DB21, see their Fig. 8d).

As soon as differences arise in low-level thermodynamic variables such as 2-m temperature and 2-m specific humidity, instability quantities will also be affected (i.e., CAPE and CIN). The summer average CAPE (JJA, 2016–18) computed from the daily WRF$_S$ output (Fig. 6a) exhibits a gradient from northwest to southeast with minimal values west of the Rocky Mountains and maximum quantities along the eastern and
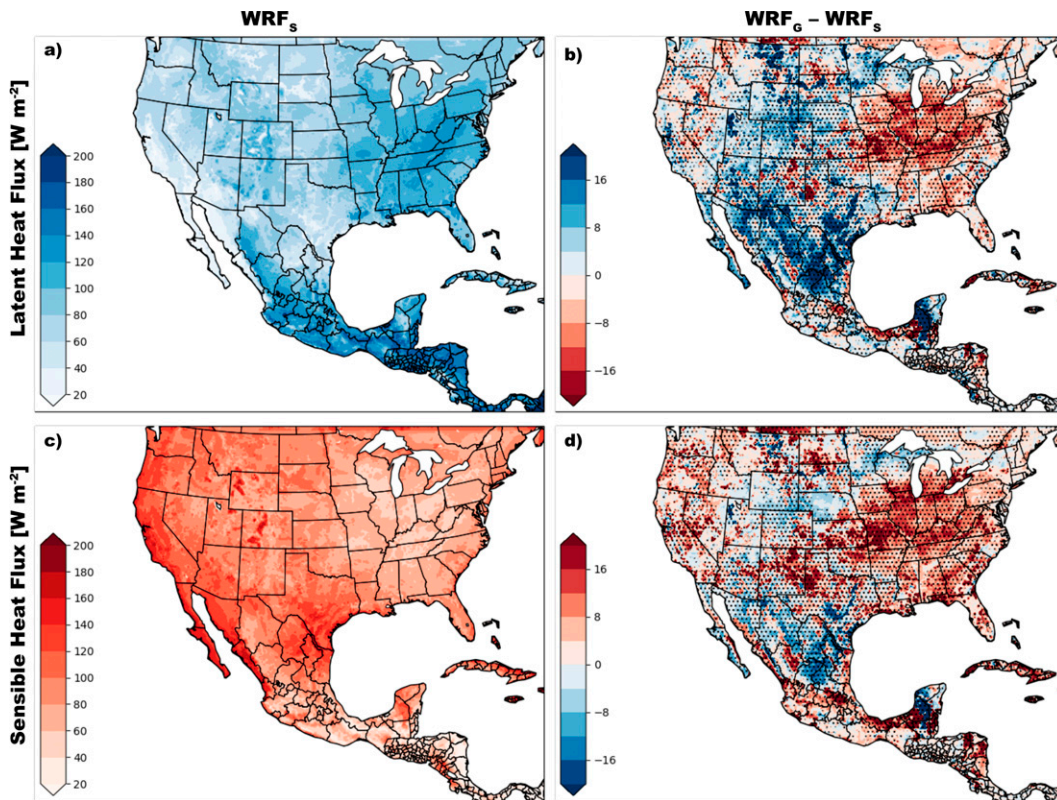
FIG. 5. Three-year JJA-averaged surface (a) latent heat flux (W m^{-2}) and (c) sensible heat flux (W m^{-2}) maps are shown for the WRF$_S$ simulation as well as the differences (WRF$_G$ − WRF$_S$) in (b) latent heat flux and (d) sensible heat flux. The stippled areas in (b) and (d) denote statistically significant differences in daily values at the 95% confidence interval ($p = 0.05$).

southern coasts. The primary feature in the CAPE differences map (WRF$_G$ − WRF$_S$; Fig. 6b) is an area of reduced mean daily CAPE in the upper Midwest of 150–200 J kg^{-1} (i.e., 15%–20% of the climatological value in that region). These differences in mean CAPE are statistically significant ($p = 0.05$) in the area collocated with the main differences in surface fluxes (see stipples in Fig. 6b). The smaller soil grains in WRF$_G$ lead to reduced 2-m temperature and increased 2-m temperature as discussed in DB21. These warmer and drier conditions related to the finer soil grains lead to a reduction in CAPE and, therefore, less conducive conditions for convection initiation and maintenance.

The JJA 2016–18 mean pattern in CIN is slightly different from the CAPE pattern in the WRF$_S$ simulation for this period (Fig. 6c). The eastern United States shows more elevated values than the western United States, similar to CAPE; however, CIN's maximum values occur in the Great Plains (about 200 J kg^{-1}). The differences (WRF$_G$ − WRF$_S$; Fig. 6d) in CIN display a considerable reduction of CIN in an area similar to and just west of CAPE's negative differences. This area of differences in Fig. 6d is mostly statistically significant at a 95% confidence interval ($p = 0.05$). CIN's value can be based on either temperature or moisture depending on the ratio of the environmental stratification to the moist potential temperature lapse rate (Crook 1996).

That is, it depends on the lapse rate between the LCL and the LFC. The warmer and drier surface environment in the WRF$_G$ simulation would increase the LCL height and reduce the distance between it and the LFC, in some cases, reducing CIN.

The differences in CAPE and CIN can be traced directly to the impact of reducing the soil grain size in the WRF$_G$ simulation. Taken together, the differences indicate that the WRF$_G$ environment has less energy available to sustain convection (CAPE: from −150 to 200 J kg^{-1}), yet, in the Midwest, that energy is more easily accessible (CIN: −50 J kg^{-1}), resulting in a competing effect for precipitation processes. The differences in CIN and, especially in CAPE, are related to the differences in surface fluxes; therefore, they can also be related to soil hydrophysical properties via soil texture.

b. Moisture transports

The implications of changing the soil's hydrophysical properties extend beyond creating conducive or inhibited convective environments. By changing the structure and evolution of the PBL through adjusting the distribution of soil properties, low-level circulation and moisture transports are also affected. To evaluate these processes, integrated quantities are presented in Fig. 7: precipitable water and moisture transports. Mean
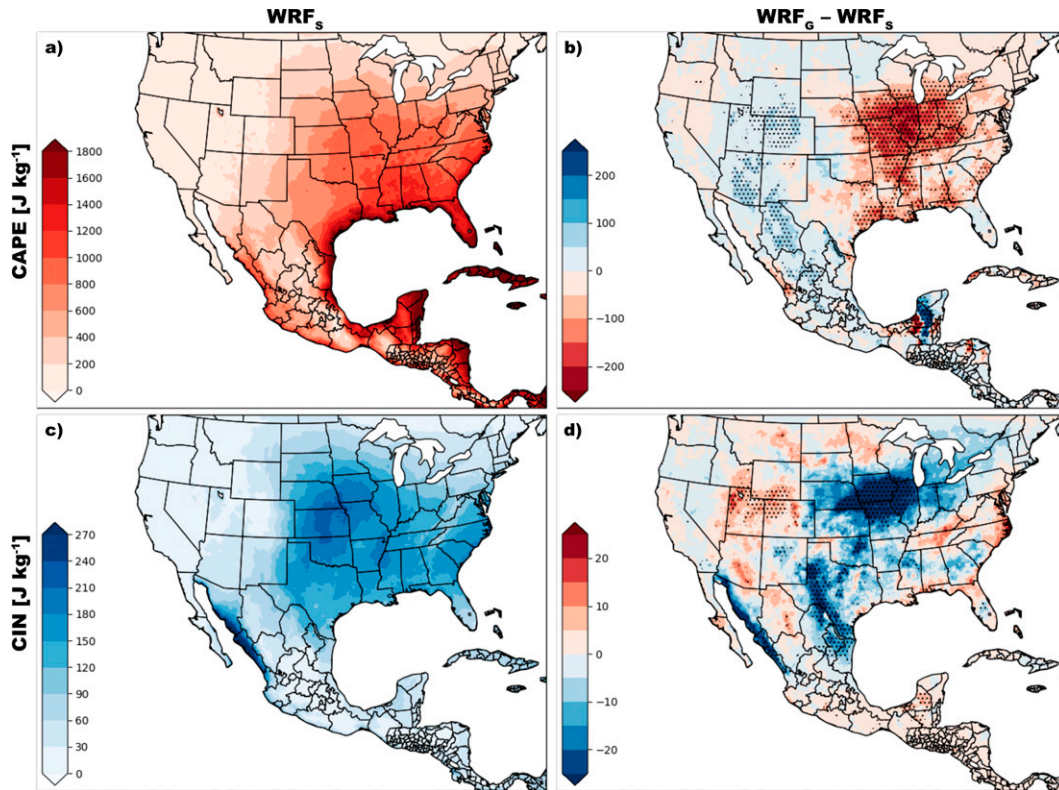
FIG. 6. Three-year JJA-averaged (a) CAPE (J kg^{-1}) and (c) CIN (J kg^{-1}) maps are shown for the WRF$_S$ simulation as well as the differences (WRF$_G$ − WRF$_S$) in (b) CAPE and (d) CIN. Stippled areas in (b) and (d) represent statistically significant differences at $p = 0.05$.

values in the figure are consistent with previous analysis (e.g., Roads et al. 1994).

Precipitable water in the WRF$_S$ simulation increases from the western deserts to the southeastern coastal regions (Fig. 7a), with the highest values occurring along the Gulf of Mexico coast in Florida and in the Yucatan Peninsula. The precipitable water differences (WRF$_G$–WRF$_S$; Fig. 7b) describe a similar pattern to the differences in latent heat flux (Fig. 5b) with negative values occurring throughout the Midwest, again consistent with the area of smaller soil grain sizes. The finer soil grains in this region restrict evaporation and lead to drier conditions above the surface. Additionally, there are positive differences in precipitable water throughout central Mexico and extending northward along the Rocky Mountains toward northeastern Colorado and western Nebraska.

The WRF$_S$ moisture transports are shown in Fig. 7c (vectors), while the WRF$_G$ − WRF$_S$ differences are shown in Fig. 7d with red vectors indicating statistically significant values ($p = 0.1$). The moisture transport vectors are calculated by multiplying water vapor (q) by the u and v wind components at each level and then integrating vertically. The vectors (1 shown every 20 grid points) indicate strong southerly flow from the Gulf of Mexico into the central United States, a feature consistent with the Great Plains low-level jet location. At the terminus of the low-level jet, the vectors veer eastward into the Midwest and progress to the East Coast, eventually continuing to wrap

southward toward the southern Appalachian Mountains and the U.S. Southeast.

Figure 7d shows that changes in the soil properties induce differences in moisture transports (vectors). The WRF$_G$ simulations show an increased southerly flow of moisture toward the Rocky Mountains, an area consistent with the positive differences in precipitable water (Fig. 7a). These differences emanate from central Mexico, a place of increased soil grain size in the WRF$_G$ simulation. The differences in moisture transports in the Midwest indicate a northward extension of the Great Plains low-level jet and concurrent veering throughout Nebraska and extension northeastward toward Wisconsin and Indiana. These differences are statistically significant at the 90% level ($p = 0.1$) denoted by the red vectors in Fig. 7d. The vectors along the eastern coastal region show enhanced northerly transport of moisture. Along southern coastal United States, it shows enhanced easterly transport of moisture culminating in a net cyclonic circulation of moisture transports in the eastern United States encircling the area of finer soil grains in the WRF$_G$ simulation.

In general, the larger sensible heat flux in the WRF$_G$ simulations (Fig. 5d) instigates enhanced turbulent kinetic energy in the boundary layer leading to higher planetary boundary layer heights. The interaction of this PBL structure with the low-level winds can lead to either enhanced or diminished horizontal flows at a given height, as seen here. This agrees
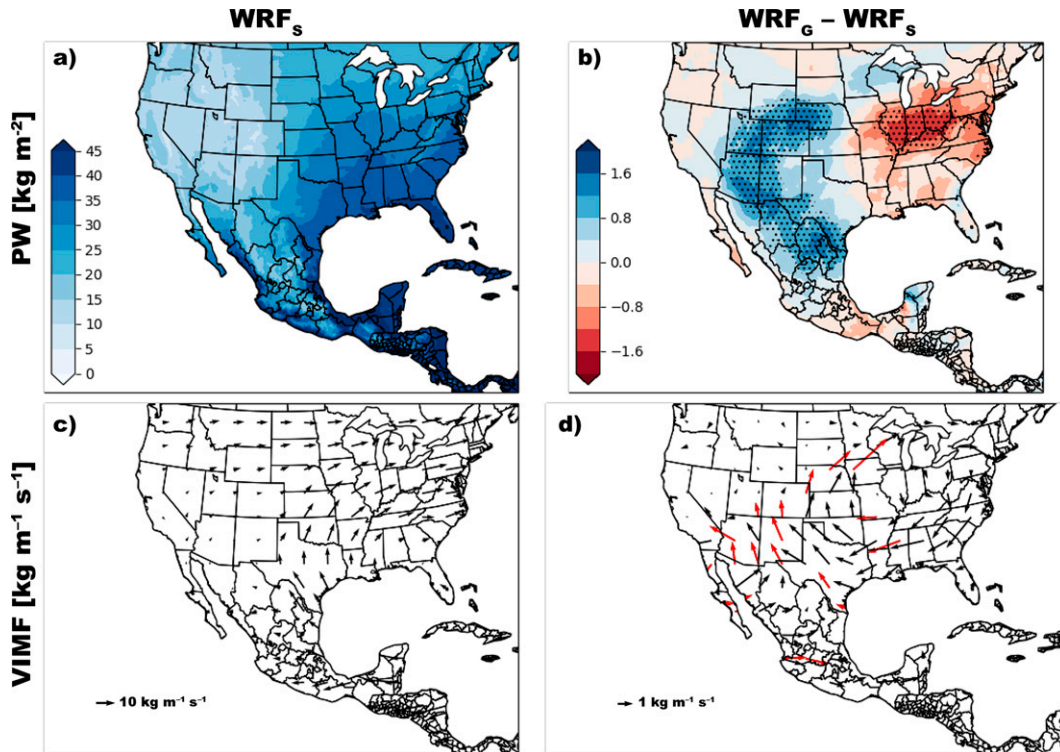
FIG. 7. (a),(c) Three-year JJA-averaged quantities are shown for the WRF$_S$ simulation and (b),(d) the differences (WRF$_G$ − WRF$_S$) in those quantities. (top) Precipitable water (kg m^{-2}) and (bottom) vertically integrated moisture flux vectors every 20 grid spaces (kg m s^{-1}; see keys for standard vector sizes). Stippled areas in (b) and red vectors in (d) show 90% confidence intervals ($p = 0.1$).

with previous findings where warm anomalies can lead to enhanced meridional moisture transports (Yang and Dominguez 2019). Furthermore, moisture transports are predominantly low-level phenomena because most atmospheric moisture is in the lower troposphere. In some cases, the height of the strongest winds in the boundary layer is altered, resulting in an alignment of strong winds and high moisture content, therefore, enhancing moisture transports (such as in Iowa and Illinois in WRF$_G$). In other cases, the height of the strongest winds is separated from the concentrated moisture, leading to reduced moisture transports (such as along the Gulf Coast in WRF$_G$). In both cases, the corridors of intense winds and the areas of enhanced moisture in the PBL are directly influenced by surface moisture and energy fluxes, which have been altered by changing the soil texture assignments.

c. Atmospheric water budget

The primary components of the atmospheric moisture budget are precipitation (P), evapotranspiration (ET), and the vertically integrated moisture flux convergence (MFC) can be related as

$$\text{MFC} = \text{ET} - P + R, \tag{1}$$

where R is a residual term. MFC in Eq. (1) is given by

$$\text{MFC} = \nabla \cdot \frac{1}{g} \int_{P_{\text{top}}}^{P_{\text{sfc}}} (q\mathbf{V}) \, dp, \tag{2}$$

where q is water vapor, $\mathbf{V}$ is the vector wind field, and g is gravity; the integral is computed on pressure coordinates. Commonly, the change in water content in an atmospheric column over time is also included ($\partial W/\partial t$) in the atmospheric water budget, but this term is much smaller than the other three, so it is left out of this first-order analysis.

This simple budget equation states that the moisture entering a given volume of air (by moisture flux convergence and evapotranspiration) is equal to the water exiting that volume (by precipitation). It is a relationship that has been fundamental to water budget studies for decades (Rasmusson 1968; Roads et al. 1994; Berbery et al. 1996; Berbery and Rasmusson 1999; Li et al. 2013; Trenberth et al. 2007). The individual terms of Eq. (1) are shown in Fig. 8, and the values over the Midwest region are expressed in Table 2.

Figure 8a shows the (JJA 2016–18) mean precipitation from the WRF$_S$ simulation. The largest precipitation is found over southern Mexico and Central America, followed by large values in areas of topography (the Rocky Mountains and throughout the Appalachian Region), and there is generally increasing precipitation from the Rocky Mountains eastward to the Atlantic and Gulf Coasts like the NLDAS forcing (Fig. 4a) but with smaller values. The differences due to soil
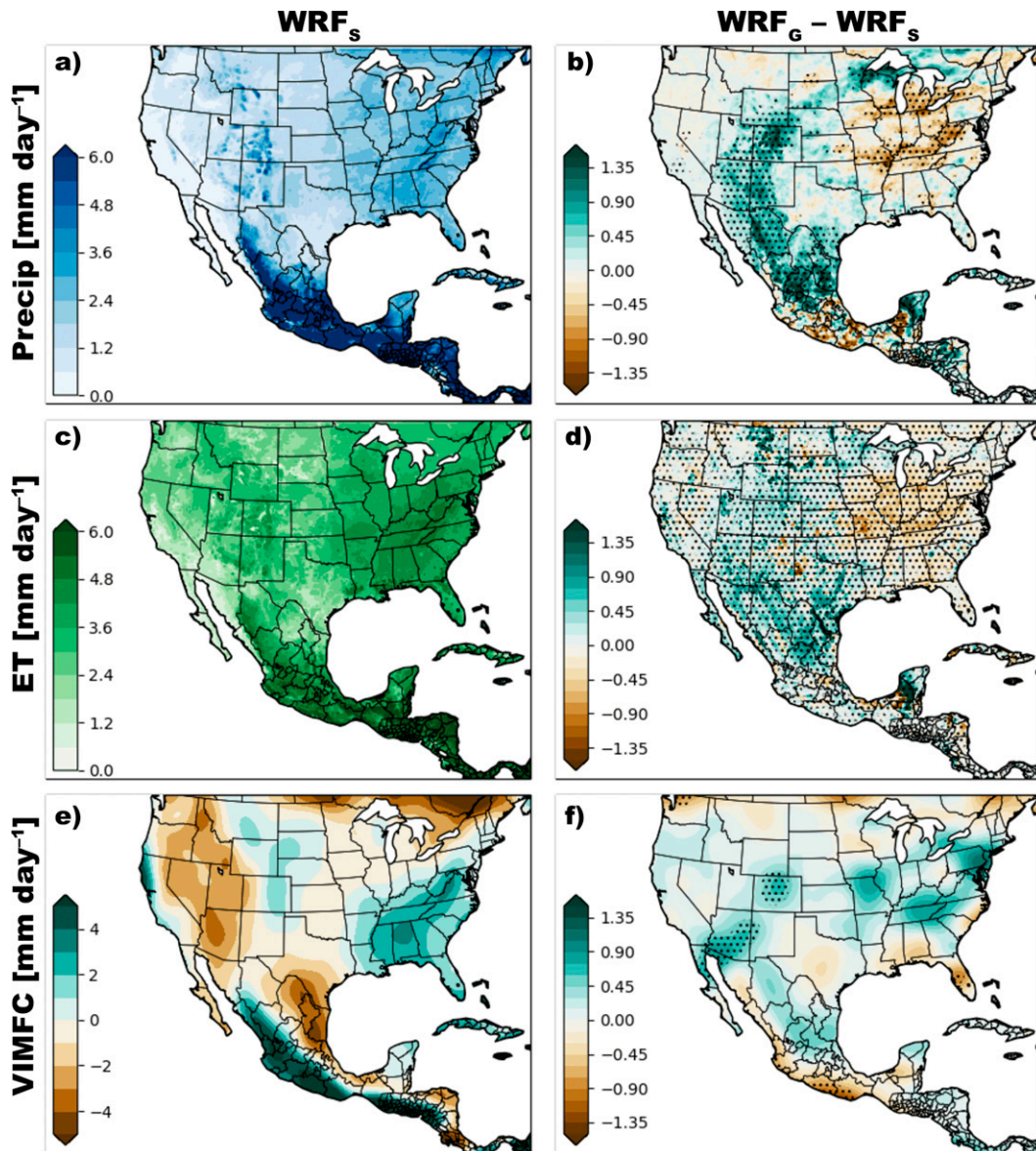
FIG. 8. The main components of the 3-yr JJA-averaged atmospheric water budget are displayed for the WRF_S simulation: (a) P, (c) ET, and (e) MFC; while the differences ($WRF_G - WRF_S$) in simulation-averaged quantities are shown: (b) P, (d) ET, and (f) MFC. All units are mm day^{-1}. Stippled areas (b), (d), and (f) show 90% confidence intervals ($p = 0.1$).

texture changes in the simulations ($WRF_G - WRF_S$; Fig. 8b) depict positive P values throughout the Rocky Mountains. These differences in precipitation in both the western United States and many of the negative differences in the eastern United States are statistically significant at $p = 0.1$. The differences in precipitation are collocated with statistically significant differences in runoff of the same signs (not shown). The runoff then acts to redistribute moisture at the surface, which in turn can affect surface fluxes and streamflow.

Three-year JJA-averaged ET from the WRF_S simulation is represented in Fig. 8c, with the ET differences ($WRF_G - WRF_S$) are presented in Fig. 8d. The highest values of ET in WRF_S are located along the Appalachian Mountains, with

maximum values nearing 4.5 mm day^{-1}. The largest continuous area of negative differences is collocated with the area of decreasing soil grain size in the Midwestern United States (Fig. 1c). The largest continuous area of negative ET differences (Fig. 8d) is also collocated with the largest negative differences in P (Fig. 8b). Differences in ET are strongly linked to the changes in soil texture categories supported by the widespread areas of statistical significance (Fig. 8d). Enhanced ET modifies the thermodynamic instability (i.e., CAPE/CIN; Fig. 6) to create an environment more or less conducive for precipitation.

In WRF_G, the ET is reduced due to the soil's hydrophysical properties creating drier conditions above the surface (Fig. 8c). This leads to negative differences in CAPE (Fig. 6b) in the same

TABLE 2. The main components of the atmospheric water budget are shown from the Midwest: precipitation (P), moisture flux convergence (MFC), evapotranspiration (ET), and the residual (RES). Single-month averages are included as well as the full-period means. All units are mm day^{-1}.

3-yr mean	WRF$_S$				WRF$_G$			
	P	MFC	ET	Res	P	MFC	ET	Res
June	2.95	0.55	4.72	1.22	2.83	0.67	4.56	1.06
July	2.55	0.92	4.12	0.64	1.98	1.11	3.64	0.55
August	1.81	1.17	2.87	−0.11	1.57	1.84	2.52	−0.89
Total	2.44	0.88	3.90	0.58	2.13	1.21	3.57	0.24

region. The differences in ET (about 1 mm day^{-1}) represent about 20% of the simulation-average value of ET. The differences in precipitation in this area (about 0.75–1.0 mm day^{-1}) consequently also represent about 20% of the 3-yr JJA-averaged value.

Moisture flux convergence for WRF$_S$ is shown in Fig. 8e, and differences between the model simulations are shown in Fig. 8f. MFC has been smoothed using a two-dimensional Gaussian smoother based on the standard deviation of the raw field. Its differences tend to agree with the differences in P: in central Mexico, positive differences in MFC are collocated with positive P differences. Similarly, there are modest positive and statistically significant differences in MFC throughout the Rocky Mountains in an area where there are also positive differences in P. However, in the eastern United States, particularly in the Midwest, the precipitation differences (WRF$_G$ − WRF$_S$) are primarily negative despite (not significant) positive differences in MFC. MFC can be influenced by both dynamic (**V**) and thermodynamic (q) factors. Following the methodology of Chen et al. (2019), we separated the thermodynamic component from the dynamic component of the vertically integrated vertical advection of moisture and found that indeed it was mostly dynamic in nature (not shown), despite some minor thermodynamic signatures. While in principle this result seems counterintuitive, it is because other elements come into play.

MFC is one of the factors determining precipitation, but not the only one. To better understand the processes involved, we examine the thermodynamic factors. The negative differences in P are in (and just east of) the statistically significant region of reduced mean CAPE (Fig. 6b). In the Midwest, there appears to be a higher correspondence between the differences in CAPE (Fig. 6b) and precipitation (Fig. 8a), than there is between MFC (Fig. 8f) and precipitation suggesting that precipitation in this region may be more sensitive to thermodynamic instability than it is to moisture flux convergence. Nonetheless, this study shows that through the changes in soil hydrophysical properties, the boundary layer is altered, affecting the low-level winds and the general circulation as it applies to the atmospheric water budget.

5. Conclusions

This study explored the effects of soil hydrophysical properties on surface fluxes and subsequently on atmospheric

stability and the atmospheric water budget. To this end, 3-yr JJA regional WRF simulations employing different external soil texture databases were conducted. First, the well-known soil databases, STATSGO and GSDE, are used to assign soil texture categories to model grid spaces. Those assignments are used with an accompanying lookup table to insert the appropriate soil hydrophysical property when necessary. Look-up tables are convenient from a computing efficiency standpoint. Still, they assume that soil properties associated with a soil texture category in one location are the same as that category's properties everywhere, which is not always the case. By changing the external soil database, the spatial patterns of the soil's hydrophysical properties are changed. Therefore, they affect the interactions between surface and subsurface moisture and the atmosphere.

The STATSGO dataset is contrasted against the GSDE dataset using RCMs to infer the impact of soil texture on land atmosphere interactions and the atmospheric moisture budget. These two datasets represent premier estimates of soil texture, and each is widely used. However, as is evident in Fig. 1, they exhibit substantial differences. Most notably, the GSDE dataset represents a reduction in soil grain size throughout the Midwest.

It has been shown that reducing the soil grain size leads to a reduction in latent heat flux and an increase in sensible heat flux for a given value of soil moisture (DB21). The changes in fluxes via soil texture altered low-level humidity and temperature leading to differences in 3-yr JJA-averaged thermodynamic instability characteristics. In the Midwest, the WRF$_G$ environment experienced a statistically significant drop in mean CAPE. Reduction in CAPE signifies a reduction in energy available to sustain convection. However, that area and areas just west of the Midwest also experienced a statistically significant reduction in CIN. The net effect of reducing both CIN and CAPE is an environment with less energy to sustain convection (smaller CAPE); yet, that energy is more easily accessed (smaller CIN), resulting in a competing effect for precipitation processes. The location of the precipitation differences suggests a closer relationship to the differences in CAPE than to the differences in CIN.

Changes in surface fluxes due to the soil's hydrophysical properties also have dynamical implications, affecting atmospheric moisture transports and vertically integrated moisture flux convergence. Differences in sensible heat flux lead to changes in turbulent kinetic energy and PBL growth. In this case, those interactions led to enhanced horizontal flows, such that a main general circulation feature, the Great Plains low-level jet, was elongated, and in the exit region, the WRF$_G$ simulation indicated stronger veering into the upper Midwest. Similarly, along the southern coastal states and just inland, there was a net easterly return flow, connecting a net cyclonic rotation of moisture transports encircling the area of reduced soil grain size in the WRF$_G$ simulation.

Furthermore, it has been shown that changing the soil hydrophysical properties can affect each term in the atmospheric water budget: P, ET, and MFC. The largest differences were shown in seasonal mean ET, a direct relationship in which smaller soil grains lead to reduced ET via the

mechanisms described in DB21. Lesser but still apparent differences were found in MFC that are related to two mechanisms: 1) soil-related differences in low-level atmospheric moisture and 2) differences in low-level horizontal winds related to soil-modulated surface heat fluxes. Using the approach from Chen et al. (2019), it is demonstrated that the differences in MFC are primarily dynamic in nature (not shown).

Furthermore, the changes in continental precipitation depend on the type of precipitation regime: ones that resemble and appear to be dependent on MFC (i.e., arid regions throughout Mexico and the Rocky Mountains), and ones that are more dependent on the thermodynamic instability (i.e., the Midwest). The arid mountain west is strongly dependent on atmospheric transport of moisture before precipitation, otherwise there is not sufficient moisture available. On the hand, in the Midwest, there is usually sufficient moisture available for precipitation to occur, but it may be inhibited by thermodynamic instability. In both scenarios, atmospheric transport of moisture occurs, but it is more critical in the mountain west. In either case, both regimes can be affected by soil properties through the various mechanism. Finally, the results of this study suggest that uncertainties in the definition of soil hydrophysical properties can lead to differences of the order of 15%–20% of the mean values in the atmospheric water budget in summer.

REFERENCES

Avissar, R., and Y. Liu, 1996: Three-dimensional numerical study of shallow convective clouds and precipitation induced by land surface forcing. *J. Geophys. Res.*, **101**, 7499–7518, https://doi.org/10.1029/95JD03031.

Berbery, E. H., and E. M. Rasmusson, 1999: Mississippi moisture budgets on regional scales. *Mon. Wea. Rev.*, **127**, 2654–2673, https://doi.org/10.1175/1520-0493(1999)127<2654:MMBORS>2.0.CO;2.

——, ——, and K. E. Mitchell, 1996: Studies of North American continental-scale hydrology using Eta model forecast products. *J. Geophys. Res.*, **101**, 7305–7319, https://doi.org/10.1029/95JD02373.

Biraud, S., M. Fischer, S. Chan, and M. Torn, 2020: AmeriFlux US-ARM ARM Southern Great Plains site- Lamont, Ver. 10-5. AmeriFlux AMP, accessed 7 August 2020, https://doi.org/10.17190/AMF/1246027.

Bonan, G. B., E. G. Patton, I. N. Harman, K. W. Oleson, J. J. Finnigan, Y. Lu, and E. A. Burakowski, 2018: Modeling canopy-induced turbulence in the Earth system: A unified parameterization of turbulent exchange within plant canopies and the roughness sublayer (CLM-ml v0). *Geosci. Model Dev.*, **11**, 1467–1496, https://doi.org/10.5194/gmd-11-1467-2018.

Bosilovich, M. G., and W. Sun, 1998: Monthly simulation of surface layer fluxes and soil properties during FIFE. *J. Atmos. Sci.*, **55**, 1170–1184, https://doi.org/10.1175/1520-0469(1998)055<1170:MSOSLF>2.0.CO;2.

Breuer, H., F. Ács, B. Laza, Á. Horváth, I. Matyasovszky, and K. Rajkai, 2012: Sensitivity of MM5-simulated planetary boundary layer height to soil dataset: Comparison of soil and atmospheric effects. *Theor. Appl. Climatol.*, **109**, 577–590, https://doi.org/10.1007/s00704-012-0597-y.

Cai, X., Z.-L. Yang, Y. Xia, M. Huang, H. Wei, L. R. Leung, and M. B. Ek, 2014: Assessment of simulated water balance from Noah, Noah-MP, CLM, and VIC over CONUS using the NLDAS test bed. *J. Geophys. Res. Atmos.*, **119**, 13 751–13 770, https://doi.org/10.1002/2014JD022113.

Chaney, N. W., and Coauthors, 2019: POLARIS Soil Properties: 30-m probabilistic maps of soil properties over the contiguous United States. *Water Resour. Res.*, **55**, 2916–2938, https://doi.org/10.1029/2018WR022797.

Chen, C., and Coauthors, 2019: Thermodynamic and dynamic responses to deforestation in the maritime continent: A modeling study. *J. Climate*, **32**, 3505–3527, https://doi.org/10.1175/JCLI-D-18-0310.1.

Cosby, B. J., G. M. Hornberger, R. B. Clapp, and T. R. Ginn, 1984: A statistical exploration of the relationships of soil moisture characteristics to the physical properties of soils. *Water Resour. Res.*, **20**, 682–690, https://doi.org/10.1029/WR020i006p00682.

Cosgrove, B. A., and Coauthors, 2003: Real-time and retrospective forcing in the North American Land Data Assimilation System (NLDAS) project. *J. Geophys. Res.*, **108**, 8842, https://doi.org/10.1029/2002JD003118.

Crook, N. A., 1996: Sensitivity of moist convection forced by boundary layer processes to low-level thermodynamic fields. *Mon. Wea. Rev.*, **124**, 1767–1785, https://doi.org/10.1175/1520-0493(1996)124<1767:SOMCFB>2.0.CO;2.

Dai, Y., and Coauthors, 2019a: A global high-resolution data set of soil hydraulic and thermal properties for land surface modeling. *J. Adv. Model. Earth Syst.*, **11**, 2996–3023, https://doi.org/10.1029/2019MS001784.

——, and Coauthors, 2019b: A review of the global soil property maps for Earth system models. *Soil*, **5**, 137–158, https://doi.org/10.5194/soil-5-137-2019.

de Lannoy, G. J. M., R. D. Koster, R. H. Reichle, S. P. P. Mahanama, and Q. Liu, 2014: An updated treatment of soil texture and associated hydraulic properties in a global land modeling system. *J. Adv. Model. Earth Syst.*, **6**, 957–979, https://doi.org/10.1002/2014MS000330.

Dennis, E. J., and E. H. Berbery, 2021: The role of soil texture in local land surface–atmosphere coupling and regional climate. *J. Hydrometeor.*, **22**, 313–330, https://doi.org/10.1175/JHM-D-20-0047.1.

Dirmeyer, P. A., 2011: The terrestrial segment of soil moisture–climate coupling. *Geophys. Res. Lett.*, **38**, L16702, https://doi.org/10.1029/2011GL048268.

Dirmeyer, P., Z. Wang, M. J. Mbuh, and H. E. Norton, 2014: Intensified land surface control on boundary layer growth in a changing climate. *Geophys. Res. Lett.*, **41**, 1290–1294, https://doi.org/10.1002/2013GL058826.

Duffková, R., , 2013: Influence of soil physical properties and terrain relief on actual evapotranspiration in the catchment with prevailing arable land determined by energy balance and Bowen ratio. *Evapotranspiration—An Overview*, IntechOpen, https://doi.org/10.5772/52810.

Ek, M., and R. H. Cuenca, 1994: Variation in soil parameters: Implications for modeling surface fluxes and atmospheric boundary-layer development. *Bound.-Layer Meteor.*, **70**, 369–383, https://doi.org/10.1007/BF00713776.

Eltahir, E. A. B., 1998: A soil moisture–Rainfall feedback mechanism: 1. Theory and observations. *Water Resour. Res.*, **34**, 765–776, https://doi.org/10.1029/97WR03499.

FAO/UNSECO, 1971: The FAO-UNESCO Soil Map of the World. https://www.fao.org/soils-portal/data-hub/soil-maps-and-databases/faounesco-soil-map-of-the-world/en/.

Findell, K. L., and E. A. B. Eltahir, 1997: An analysis of the soil moisture-rainfall feedback, based on direct observations from Illinois. *Water Resour. Res.*, **33**, 725–735, https://doi.org/10.1029/96WR03756.

Fisher, R. A., and C. D. Koven, 2020: Perspectives on the future of land surface models and the challenges of representing complex terrestrial systems. *J. Adv. Model. Earth Syst.*, **12**, e2018MS001453, https://doi.org/10.1029/2018MS001453.

Hengl, T., and Coauthors, 2017: SoilGrids250m: Global gridded soil information based on machine learning. *PLOS ONE*, **12**, e0169748, https://doi.org/10.1371/journal.pone.0169748.

Hohenegger, C., P. Brockhaus, C. S. Bretherton, and C. Schär, 2009: The soil moisture–precipitation feedback in simulations with explicit and parameterized convection. *J. Climate*, **22**, 5003–5020, https://doi.org/10.1175/2009JCLI2604.1.

Holt, T. R., D. Niyogi, F. Chen, K. Manning, M. A. LeMone, and A. Qureshi, 2006: Effect of land–atmosphere interactions on the IHOP 24–25 May 2002 convection case. *Mon. Wea. Rev.*, **134**, 113–133, https://doi.org/10.1175/MWR3057.1.

Iacono, M. J., J. S. Delamere, E. J. Mlawer, M. W. Shephard, S. A. Clough, and W. D. Collins, 2008: Radiative forcing by long-lived greenhouse gases: Calculations with the AER radiative transfer models. *J. Geophys. Res.*, **113**, D13103, https://doi.org/10.1029/2008JD009944.

Janjić, Z. I., J. P. Gerrity Jr., and S. Nickovic, 2001: An alternative approach to nonhydrostatic modeling. *Mon. Wea. Rev.*, **129**, 1164–1178, https://doi.org/10.1175/1520-0493(2001)129<1164:AAATNM>2.0.CO;2.

Kim, C. P., and D. Entekhabi, 1998: Impact of soil heterogeneity in a mixed-layer model of the planetary boundary layer. *Hydrol. Sci. J.*, **43**, 633–658, https://doi.org/10.1080/02626669809492158.

Kishné, A. S., Y. T. Yimam, C. L. S. Morgan, and B. C. Dornblaser, 2017: Evaluation and improvement of the default soil hydraulic parameters for the Noah land surface model. *Geoderma*, **285**, 247–259, https://doi.org/10.1016/j.geoderma.2016.09.022.

Koster, R. D., and Coauthors, 2004: Regions of strong coupling between soil moisture and precipitation. *Science*, **305**, 1138–1140, https://doi.org/10.1126/science.1100217.

Ladwig, W., 2017: NCAR/wrf-python. National Center for Atmospheric Research, https://doi.org/10.5065/D6W094P1.

Lawrence, D. M., P. E. Thornton, K. W. Oleson, and G. B. Bonan, 2007: The partitioning of evapotranspiration into transpiration, soil evaporation, and canopy evaporation in a GCM: Impacts on land–atmosphere interaction. *J. Hydrometeor.*, **8**, 862–880, https://doi.org/10.1175/JHM596.1.

——, and Coauthors, 2011: Parameterization improvements and functional and structural advances in Version 4 of the Community Land Model. *J. Adv. Model. Earth Syst.*, **3**, M03001, https://doi.org/10.1029/2011MS00045.

Lee, J. M., Y. Zhang, and S. A. Klein, 2019: The effect of land surface heterogeneity and background wind on shallow cumulus clouds and the transition to deeper convection. *J. Atmos. Sci.*, **76**, 401–419, https://doi.org/10.1175/JAS-D-18-0196.1.

Lee, S.-J., and E. H. Berbery, 2012a: Land cover change effects on the climate of the La Plata basin. *J. Hydrometeor.*, **13**, 84–102, https://doi.org/10.1175/JHM-D-11-021.1.

——, and ——, 2012b: Land cover change effects on the climate of the La Plata basin. *J. Hydrometeor.*, **13**, 84–102, https://doi.org/10.1175/JHM-D-11-021.1.

——, ——, and D. Alcaraz-Segura, 2013: The impact of ecosystem functional type changes on the La Plata Basin climate. *Adv. Atmos. Sci.*, **30**, 1387–1405, https://doi.org/10.1007/s00376-012-2149-x.

Lehmann, P., O. Merlin, P. Gentine, and D. Or, 2018: Soil texture effects on surface resistance to bare-soil evaporation. *Geophys. Res. Lett.*, **45**, 10 398–10 405, https://doi.org/10.1029/2018GL078803.

Li, L., W. Li, and A. P. Barros, 2013: Atmospheric moisture budget and its regulation of the summer precipitation variability over the Southeastern United States. *Climate Dyn.*, **41**, 613–631, https://doi.org/10.1007/s00382-013-1697-9.

Liao, K.-H., L.-G. Lv, G.-S. Yang, and Q. Zhu, 2016: Sensitivity of simulated hillslope subsurface flow to rainfall patterns, soil texture and land use. *Soil Use Manage.*, **32**, 422–432, https://doi.org/10.1111/sum.12282.

Lu, D., H. Wang, D. Huang, D. Li, and Y. Sun, 2020: Measurement and estimation of water retention curves using electrical resistivity data in porous media. *J. Hydrol. Eng.*, **25**, 04020021, https://doi.org/10.1061/(ASCE)HE.1943-5584.0001925.

Matamala, R., 2019: AmeriFlux US-IB1 Fermi National Accelerator Laboratory- Batavia (Agricultural site), Ver. 8-5. AmeriFlux AMP, accessed 7 August 2020, https://doi.org/10.17190/AMF/1246065.

Mesinger, F., and Coauthors, 2006: North American Regional Reanalysis. *Bull. Amer. Meteor. Soc.*, **87**, 343–360, https://doi.org/10.1175/BAMS-87-3-343.

Mu, M., and Coauthors, 2021: Evaluating a land surface model at a water-limited site: Implications for land surface contributions to droughts and heatwaves. *Hydrol. Earth Syst. Sci.*, **25**, 447–471, https://doi.org/10.5194/hess-25-447-2021.

Müller, O. V., E. H. Berbery, D. Alcaraz-Segura, and M. B. Ek, 2014: Regional model simulations of the 2008 drought in southern South America using a consistent set of land surface properties. *J. Climate*, **27**, 6754–6778, https://doi.org/10.1175/JCLI-D-13-00463.1.

Nakanishi, M., and H. Niino, 2006: An improved Mellor–Yamada level-3 model: Its numerical stability and application to a regional prediction of advection fog. *Bound.-Layer Meteor.*, **119**, 397–407, https://doi.org/10.1007/s10546-005-9030-8.

Navale, A., C. Singh, S. Budakoti, and S. K. Singh, 2020: Evaluation of season long rainfall simulated by WRF over the NWH region: KF vs. MSKF. *Atmos. Res.*, **232**, 104682, https://doi.org/10.1016/j.atmosres.2019.104682.

Novick, K., and R. Phillips, 2020: AmeriFlux US-MMS Morgan Monroe State Forest, Ver. 18-5. AmeriFlux AMP, accessed 7 August 2020, https://doi.org/10.17190/AMF/1246080.

NRCS, 2012: General Soil Map (STATSGO2), Web Soil Survey. Natural Resources Conservation Service, accessed 15 September 2018, https://websoilsurvey.nrcs.usda.gov/.

Oleson, K. W., and Coauthors, 2010: Technical description of version 4.0 of the Community Land Model (CLM). NCAR Tech. Note NCAR/TN-478+STR, 257 pp., https://doi.org/10.5065/D6FB50WZ.

Or, D., and P. Lehmann, 2019: Surface evaporative capacitance: How soil type and rainfall characteristics affect global-scale surface evaporation. *Water Resour. Res.*, **55**, 519–539, https://doi.org/10.1029/2018WR024050.

Pan, H.-L., and L. Mahrt, 1987: Interaction between soil hydrology and boundary-layer development. *Bound.-Layer Meteor.*, **38**, 185–202, https://doi.org/10.1007/BF00121563.

Peters-Lidard, C. D., E. Blackburn, X. Liang, and E. F. Wood, 1998: The effect of soil thermal conductivity parameterization on surface energy fluxes and temperatures. *J. Atmos. Sci.*, **55**, 1209–1224, https://doi.org/10.1175/1520-0469(1998)055<1209:TEOSTC>2.0.CO;2.

Prats, S. A., M. C. Malvar, and J. W. Wagenbrenner, 2021: Compaction and cover effects on runoff and erosion in post-fire salvage logged areas in the Valley Fire, California. *Hydrol. Processes*, **35**, e13997, https://doi.org/10.1002/hyp.13997.

Rasmusson, E. M., 1968: Atmospheric water vapor transport and the water balance of North America: II. Large-scale water balance investigations. *Mon. Wea. Rev.*, **96**, 720–734, https://doi.org/10.1175/1520-0493(1968)096<0720:AWVTAT>2.0.CO;2.

Richards, L. A., 1931: Capillary conduction of liquids through porous mediums. *Physics*, **1**, 318–333, https://doi.org/10.1063/1.1745010.

Roads, J. O., S.-C. Chen, A. K. Guetter, and K. P. Georgakakos, 1994: Large-scale aspects of the United States hydrologic cycle. *Bull. Amer. Meteor. Soc.*, **75**, 1589–1610, https://doi.org/10.1175/1520-0477(1994)075<1589:LSAOTU>2.0.CO;2.

Santanello, J. A., and Coauthors, 2018: Land–atmosphere interactions: The LoCo perspective. *Bull. Amer. Meteor. Soc.*, **99**, 1253–1272, https://doi.org/10.1175/BAMS-D-17-0001.1.

Seneviratne, S. I., T. Corti, E. L. Davin, M. Hirschi, E. B. Jaeger, I. Lehner, B. Orlowsky, and A. J. Teuling, 2010: Investigating soil moisture–climate interactions in a changing climate: A review. *Earth-Sci. Rev.*, **99**, 125–161, https://doi.org/10.1016/j.earscirev.2010.02.004.

Shangguan, W., Y. Dai, Q. Duan, B. Liu, and H. Yuan, 2014: A global soil data set for earth system modeling. *J. Adv. Model. Earth Syst.*, **6**, 249–263, https://doi.org/10.1002/2013MS000293.

Skamarock, W. C., and Coauthors, 2008: A description of the Advanced Research WRF version 3. NCAR Tech. Note NCAR/TN-475+STR, 113 pp., https://doi.org/10.5065/D68S4MVH.

Szabó, B., G. Szatmári, K. Takács, A. Laborczi, A. Makó, K. Rajkai, and L. Pásztor, 2019: Mapping soil hydraulic properties using random-forest-based pedotransfer functions and geostatistics. *Hydrol. Earth Syst. Sci.*, **23**, 2615–2635, https://doi.org/10.5194/hess-23-2615-2019.

Thompson, G., P. R. Field, R. M. Rasmussen, and W. D. Hall, 2008: Explicit forecasts of winter precipitation using an improved bulk microphysics scheme. Part II: Implementation of a new snow parameterization. *Mon. Wea. Rev.*, **136**, 5095–5115, https://doi.org/10.1175/2008MWR2387.1.

Trenberth, K. E., L. Smith, T. Qian, A. Dai, and J. Fasullo, 2007: Estimates of the global water budget and its annual cycle using observational and model data. *J. Hydrometeor.*, **8**, 758–769, https://doi.org/10.1175/JHM600.1.

Tripathi, O. P., and F. Dominguez, 2013: Effects of spatial resolution in the simulation of daily and subdaily precipitation in the southwestern US. *J. Geophys. Res. Atmos.*, **118**, 7591–7605, https://doi.org/10.1002/jgrd.50590.

van Looy, K., and Coauthors, 2017: Pedotransfer functions in Earth system science: Challenges and perspectives. *Rev. Geophys.*, **55**, 1199–1256, https://doi.org/10.1002/2017RG000581.

Vereecken, H., and Coauthors, 2016: Modeling soil processes: Review, key challenges, and new perspectives. *Vadose Zone J.*, **15**, 1–57, https://doi.org/10.2136/vzj2015.09.0131.

Verhoef, A., and G. Egea, 2014: Modeling plant transpiration under limited soil water: Comparison of different plant and soil hydraulic parameterizations and preliminary implications for their use in land surface models. *Agric. For. Meteor.*, **191**, 22–32, https://doi.org/10.1016/j.agrformet.2014.02.009.

Wang, T., T. E. Franz, and V. A. Zlotnik, 2015: Controls of soil hydraulic characteristics on modeling groundwater recharge under different climatic conditions. *J. Hydrol.*, **521**, 470–481, https://doi.org/10.1016/j.jhydrol.2014.12.040.

Weihermüller, L., P. Lehmann, M. Herbst, M. Rahmati, A. Verhoef, D. Or, D. Jacques, and H. Vereecken, 2021: Choice of pedotransfer functions matters when simulating soil water balance fluxes. *J. Adv. Model. Earth Syst.*, **13**, e2020MS002404M, https://doi.org/10.1029/2020MS002404.

Xia, Y., and Coauthors, 2012: Continental-scale water and energy flux analysis and validation for North American Land Data Assimilation System project phase 2 (NLDAS-2): 2. Validation of model-simulated streamflow. *J. Geophys. Res.*, **117**, D03110, https://doi.org/10.1029/2011JD016051.

——, D. Mocko, M. Huang, B. Li, M. Rodell, K. E. Mitchell, X. Cai, and M. B. Ek, 2017: Comparison and assessment of three advanced land surface models in simulating terrestrial water storage components over the United States. *J. Hydrometeor.*, **18**, 625–649, https://doi.org/10.1175/JHM-D-16-0112.1.

Xie, P., M. Chen, S. Yang, A. Yatagai, T. Hayasaka, Y. Fukushima, and C. Liu, 2007: A gauge-based analysis of daily precipitation over East Asia. *J. Hydrometeor.*, **8**, 607–626, https://doi.org/10.1175/JHM583.1.

Yang, Z., and F. Dominguez, 2019: Investigating land surface effects on the moisture transport over South America with a moisture tagging model. *J. Climate*, **32**, 6627–6644, https://doi.org/10.1175/JCLI-D-18-0700.1.

Yin, J., J. D. Albertson, J. R. Rigby, and A. Porporato, 2015: Land and atmospheric controls on initiation and intensity of moist convection: CAPE dynamics and LCL crossings. *Water Resour. Res.*, **51**, 8476–8493, https://doi.org/10.1002/2015WR017286.

Yun, Y., C. Liu, Y. Luo, X. Liang, L. Huang, F. Chen, and R. Rasmmusen, 2020: Convection-permitting regional climate simulation of warm-season precipitation over Eastern China. *Climate Dyn.*, **54**, 1469–1489, https://doi.org/10.1007/s00382-019-05070-y.

Zhang, Y., M. G. Schaap, and Y. Zha, 2018: A high-resolution global map of soil hydraulic properties produced by a hierarchical parameterization of a physically based water retention model. *Water Resour. Res.*, **54**, 9774–9790, https://doi.org/10.1029/2018WR023539.

Zheng, Y., N. A. Brunsell, J. G. Alfieri, and D. Niyogi, 2021: Impacts of land cover heterogeneity and land surface parameterizations on turbulent characteristics and mesoscale simulations. *Meteor. Atmos. Phys.*, **133**, 589–610, https://doi.org/10.1007/s00703-020-00768-9.